catalysts

MDPI

Article

Evaluation of Efficient and Noble-Metal-Free $NiTiO_3$ Nanofibers Sensitized with Porous gC_3N_4 Sheets for Photocatalytic Applications

Haritham Khan, Suhee Kang and Caroline Sunyong Lee *

Department of Materials and Chemical Engineering, Hanyang University, Ansan 15588, Korea; khanhunzai@hanyang.ac.kr (H.K.); cjkkang@hanyang.ac.kr (S.K.)
* Correspondence: sunyonglee@hanyang.ac.kr; Tel.: +82-314-005-221

Abstract: One-dimensional nickel titanate nanofibers ($NiTiO_3$ NFs) were synthesized and loaded with acetic acid-treated exfoliated and sintered sheets of graphitic carbon nitride (AAs-gC_3N_4) to fabricate a unique heterogeneous structure. This novel fabrication method for porous AAs-gC_3N_4 sheets using acetic acid-treated exfoliation followed by sintering provided gC_3N_4 with a surface area manifold larger than that of bulk gC_3N_4, with an abundance of catalytically active sites. Hybrid photocatalysts were synthesized through a two-step process. Firstly, $NiTiO_3$ NFs (360 nm in diameter) were made by electrospinning, and these $NiTiO_3$ NFs were sensitized with exfoliated gC_3N_4 sheets via a sonication process. Varying the weight ratio of $NiTiO_3$ fibers to porous AAs-gC_3N_4 established that $NiTiO_3$ NFs containing 40 wt% of porous AAs-gC_3N_4 exhibited optimal activity, i.e., removal of methylene blue and H_2 evolution. After 60 min exposure to visible light irradiation, 97% of the methylene blue molecules were removed by the hybrid photocatalyst, compared with 82%, 72%, and 76% by pristine AAs-gC_3N_4, $NiTiO_3$ NFs, and bulk gC_3N_4, respectively. The optimal structure also displayed excellent H_2 evolution performance. The H_2 evolution rate in the optimal sample (152 μmol g^{-1}) was 2.2, 3.2 and 3-fold higher than that in pure AAs-gC_3N_4 (69 μmol g^{-1}), $NiTiO_3$ NFs (47 μmol g^{-1}) and bulk gC_3N_4 (50 μmol g^{-1}), respectively. This clearly shows that the holey AAs-gC_3N_4 nanosheets interacted synergistically with the $NiTiO_3$ NFs. This extended the lifetime of photogenerated charge carriers and resulted in superior photocatalytic activity compared with pristine $NiTiO_3$ NFs and bulk gC_3N_4. The higher Brunauer-Emmett-Teller surface area and the presence of many catalytically active sites also enhanced the photocatalytic performance of the hybrid sample. Moreover, through photoluminescence and photocurrent response analysis, a significant decrease in the recombination losses of the hybrid photocatalysts was also confirmed. Thus, this is a novel strategy to fabricate highly efficient photocatalysts with precisely tunable operating windows and enhanced charge separation.

Keywords: $NiTiO_3$ NFs; photocatalyst; water treatment; H_2 evolution; gC_3N_4; methylene blue

Citation: Khan, H.; Kang, S.; Lee, C.S. Evaluation of Efficient and Noble-Metal-Free $NiTiO_3$ Nanofibers Sensitized with Porous gC_3N_4 Sheets for Photocatalytic Applications. *Catalysts* **2021**, *11*, 385. https://doi.org/10.3390/catal11030385

Academic Editors: Pedro B. Tavares, Marco S. Lucas, Joaquim L. Faria and Ewa Kowalska

Received: 4 February 2021
Accepted: 15 March 2021
Published: 17 March 2021

1. Introduction

Today, with burgeoning water contamination issues and a looming energy crisis, the utilization of renewable energy is of particular interest [1]. The most efficient and ecofriendly approach to renewable energy utilization is the use of photoenergy for photocatalytic removal of pollutants and H_2 evolution via water splitting [2]. Numerous photocatalysts have been developed over the last several decades, but a more efficient photocatalyst is still needed for practical applications; low solar-to-chemical energy conversion efficiency and complex chemical reactions need to be overcome [3].

Recently, the photocatalytic activity of titanium (Ti)-based perovskite oxides, such as $SrTiO_3$, $CoTiO_3$, $ZnTiO_3$, and $NiTiO_3$, have attracted significant attention [4–7]. Nickel titanate ($NiTiO_3$) has the ilmenite structure in which both Ni and Ti have octahedral coordination with alternating cation layers occupied by Ni and Ti [8]. This titanate has

bandgap energy in the range of around 2.14 to 2.50 eV depending on the morphology, size, and synthetic route [9]. The material is highly stable in an oxidizing environment and under light irradiation. However, its low bandgap energy reduces its quantum efficiency when used as an individual photocatalyst [10].

Graphitic carbon nitride (gC_3N_4), a novel metal-free polymeric semiconductor, is another extensively used photocatalyst because of its superior photocatalytic performance [11]. However, gC_3N_4 suffers from low sunlight absorption, low quantum efficiency, and high recombination rates. Several techniques have been used to improve the photocatalytic activity of gC_3N_4 by increasing its surface area, doping, and formation of heterojunctions with other semiconductors. Many heterostructures, such as $NiTiO_3/gC_3N_4$, $NiTiO_3/TiO_2$, gC_3N_4/Bi_2WO_6, $gC_3N_4/BiOCl$, gC_3N_4/SnO_2, gC_3N_4/WO_3, $Fe_2O_3/NiTiO_3$, and gC_3N_4/ZnO [12–17], display enhanced photocatalytic activity. Notably, two-dimensional (2D) amorphous nanosheets display superior electrocatalytic performance compared with their crystalline counterparts due to the abundant active sites in amorphous structures [18]. First, the high density of well-distributed pores provides abundant active sites at the pore edges for redox reactions. Second, the abundant pores in the highly porous nanosheets can serve as permeable channels for the diffusion of reactants, thus making more subsurface materials available to be catalytically active. Third, this unique structure can shorten the diffusion lengths of photoexcited electrons from the interior to the edges for improved electron transport. The abundant interconnected pores throughout the nanosheets ensure ready access to active sites and suppress charge carrier recombination.

Morphological tuning of the material, especially one having a one-dimensional (1D) structure, can significantly improve photocatalytic activity by increasing the specific surface area and improving optical emission, electron transport, and chemical stability [19,20]. A 1D nickel titanate nanofiber ($NiTiO_3$ NF) based photocatalyst coupled with a 2D porous laminar structure would form an efficient photocatalyst addressing the intrinsic drawbacks of $NiTiO_3$ and gC_3N_4 for photocatalytic applications. To the best of our knowledge, no similar research has been reported concerning 1D/2D $NiTiO_3$/AAs-gC_3N_4-based photocatalysts for water-treatment applications [21].

Based on the above considerations, we report a cost-effective route to a unique heterostructure with enhanced photocatalytic performance formed by combining 1D $NiTiO_3$ NFs with holey 2D AAs-gC_3N_4 nanosheets. The fabrication process involved electrospinning $NiTiO_3$ NFs and their heterostructure with porous AAs-gC_3N_4 nanosheets obtained from one-step acid etching followed by thermal pyrolysis. A series of $NiTiO_3$/AAs-gC_3N_4 heterostructures, varying weight fractions were successfully fabricated and used for the removal of methylene blue (MB, a model pollutant) and H_2 evolution. The optimal combination of $NiTiO_3$/AAs-gC_3N_4 (60/40) rapidly removed MB and generated the highest H_2 yield. The improved performance was attributed to enhanced optical absorbance and efficient separation and movement of photogenerated charge carriers. This work is expected to increase interest in developing highly efficient and novel heterogeneous photocatalysts.

2. Results and Discussion

2.1. Field-Emission Scanning Electron Microscopy (FE-SEM)

The textural structure and morphology of pure $NiTiO_3$ NFs, gC_3N_4, AAs-gC_3N_4 (holey gC_3N_4), and hybrid structures were analyzed by FE-SEM (Figure 1). The observed rough-surfaced $NiTiO_3$ NFs were several micrometers long and of relatively uniform diameter (Figure 1a). Bulk gC_3N_4 consisted of disorderly stacked and irregularly sized clusters (Figure 1b), while AAs-gC_3N_4 had a loose, rough, and etched surface with abundant pores in its structure (Figure 1c). These abundant pores in AAs-gC_3N_4 serve as reaction centers by providing a large number of active sites at the pore edges and also effectively improve photogenerated carrier separation by shortening their transfer lengths. The hybrid structures were composed of $NiTiO_3$ NFs and AAs-gC_3N_4 distributed throughout the samples. High-magnification SEM images also revealed a coating of AAs-gC_3N_4 over the $NiTiO_3$ NFs (Figure 1d,e). SEM-energy-dispersive X-ray spectroscopy (Figure S1)

confirmed the presence of essential elements. The observed uniform distribution of N over the $NiTiO_3$ NFs was indicative of the coating of AAs-gC_3N_4 sheets. In addition to this coating, a separate bulky structure of AAs-gC_3N_4 was also observed. This structure may improve light absorbance and then charge separation characteristics to enhance the photocatalytic performance of the photocatalysts. It was also confirmed that AAs-gC_3N_4-rich areas concealing uncoated $NiTiO_3$ NFs were formed with increasing AAs-gC_3N_4 loading (gnT4060) (Figure 1f).

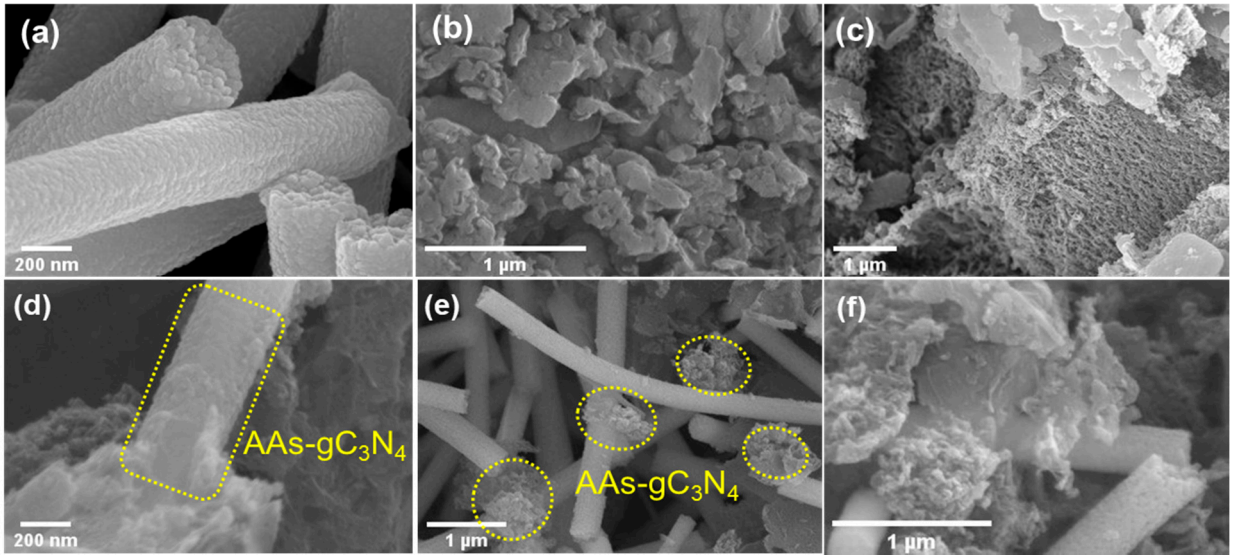

Figure 1. Field-emission scanning electron microscopy (FE-SEM) images of powder samples. (**a**) $NiTiO_3$ NFs, (**b**) bulk gC_3N_4, (**c**) AAs-gC_3N_4, (**d**,**e**) gnT6040, and (**f**) gnT4060.

2.2. Transmission Electron Microscopy (TEM) Analysis

The morphologies and crystal structures of pure $NiTiO_3$ NFs, gC_3N_4, AAs-gC_3N_4, and hybrid structures were further substantiated using TEM (Figure 2). The $NiTiO_3$ NFs had an average diameter of 360 nm. In the bulk gC_3N_4, aggregated irregular thick black particles were observed, contrary to the thin transparent porous graphene-like sheets in AAs-gC_3N_4 (Figure 2a–d).

The presence of most pores and thin layers in acid-etched gC_3N_4 was confirmed in AAs-gC_3N_4 (Figure 2d). The average pore size was approximately 14.5 nm. The presence of $NiTiO_3$ NFs with AAs-gC_3N_4 sheets in the hybrid structures was confirmed which reveals the formation of the hybrid photocatalyst. Moreover, through elemental mapping in scanning transmission electron microscopy, the $NiTiO_3$ NFs were found anchored to the surface of the AAs-gC_3N_4 sheets (Figure S5).

High magnification TEM images (Figure 2f,h) of the hybrid structures also revealed that the crystalline structure of $NiTiO_3$ NFs was maintained in the hybrid samples. A thin layer of ca. 10 nm and 13 nm of AAs-gC_3N_4 was found coated on the surface of gnT4060 and gnT6040 respectively. This uniform coverage of AAs-gC_3N_4 behaved as a junction between the fibers, as already revealed by SEM. The estimated interplanar distance in $NiTiO_3$ NFs was approximately 0.25 nm (Figure 2g), which is similar to the values already reported in the literature [22,23]. Selected area electron diffraction (Figure 2h inset) confirmed the polycrystalline nature of the hybrid structure, which was consistent with the presence of various planes of $NiTiO_3$ NFs. This close interaction between $NiTiO_3$ NFs and holey AAs-gC_3N_4 could enhance charge separation and transfer and thereby improve efficient photocatalytic activity.

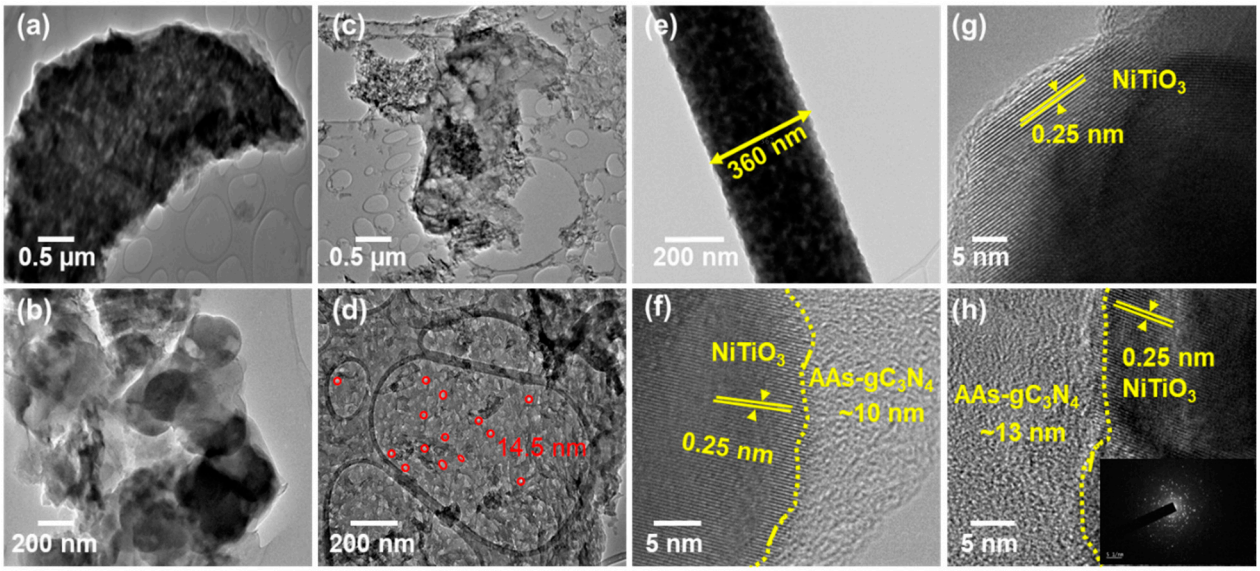

Figure 2. Transmission electron microscopy (TEM) images of the prepared samples. (**a**,**b**) Bulk gC_3N_4, (**c**,**d**) AAs-gC_3N_4 at low and high magnifications, respectively, red circles show pores in the structure with an average size of 14.5 nm (**e**,**g**) low and high magnification TEM images of $NiTiO_3$ NFs. (**f**,**h**) high magnification TEM images of gnT4060 and gnT6040 respectively.

2.3. X-ray Diffraction Analysis

The phase structures of the pristine ($NiTiO_3$ NFs, gC_3N_4, and AAs-gC_3N_4) and hybrid ($NiTiO_3$/AAs-gC_3N_4) photocatalysts were determined by X-ray diffraction analysis (Figure 3a). For the pristine $NiTiO_3$ NFs sample, the diffraction peaks at 24.1°, 33.1°, 35.7°, 49.5°, 49.5°, and 69.2° were indexed to (012), (104), (110), (024), and (208) crystal planes of ilmenite $NiTiO_3$ NFs, respectively, according to Joint Committee on Powder Diffraction Standards (JCPDS) 01-083-0198. The other two diffraction peaks observed in the $NiTiO_3$ NFs structure at 25.29° and 27.39° were attributed to the rutile (101) and anatase (110) planes TiO_2 (JCPDS card numbers 01.071-1168 and 01-076-0317, respectively). The relatively high sintering temperature (600 °C) in the air may have favored the formation of the TiO_2 phases [24]. Pristine gC_3N_4 and AAs-gC_3N_4 showed two characteristic diffraction peaks at 27.8° and 14.1°, which were associated with the (002) for conjugated aromatic segments (CN) and (100) for the structure of tri-s-triazine units in the gC_3N_4 structure, respectively [25]. The prominent peak (002) in AAs-gC_3N_4 is broader and shifted slightly towards the high-angle side as compared with that of pure gC_3N_4; this can be due to exfoliation and higher amorphous regions. The diffraction patterns of the various $NiTiO_3$/AAs-gC_3N_4 hybrid structures exhibited peaks matching the $NiTiO_3$ NFs and AAs-gC_3N_4 phases, which confirmed the hybrid structure formation. Additionally, the intensities of the $NiTiO_3$ NFs and AAs-gC_3N_4 peaks in the hybrid structures resembled those of the pristine materials, although increased loading of AAs-gC_3N_4 decreased the intensities of the $NiTiO_3$ NFs peaks. A similar trend has been reported for other gC_3N_4-based hybrids [10,26].

2.4. Fourier Transform Infrared (FT-IR) Spectroscopy Analysis

To investigate functional groups and their chemical states, FT-IR spectroscopy was used for $NiTiO_3$ NFs, gC_3N_4, AAs-gC_3N_4, and the hybrid samples (Figure 3b). Peaks observed at 455, 561, and 687 cm^{-1} were attributed to vibrations of the Ni−O, Ti−O, and Ni−O−Ti functional groups of $NiTiO_3$ NFs, respectively [27]. These peaks appeared both in the pristine and hybrid materials. The spectrum of gC_3N_4 and AAs-gC_3N_4 showed several peaks in the region of 1700−1200 cm^{-1} corresponding to the breathing mode of C−N heterocycles. The characteristic peak that appeared at 810 cm^{-1} was attributed to the hydroxyl (−OH) and the amine (−NH) groups from water molecules and the partial hydrogenation of N atoms in gC_3N_4 and AAs-gC_3N_4. The main peaks in the

heterostructures corresponded to the $NiTiO_3$ NFs and AAs-gC_3N_4 nanostructures, which provided evidence of their coexistence in a hybrid structure.

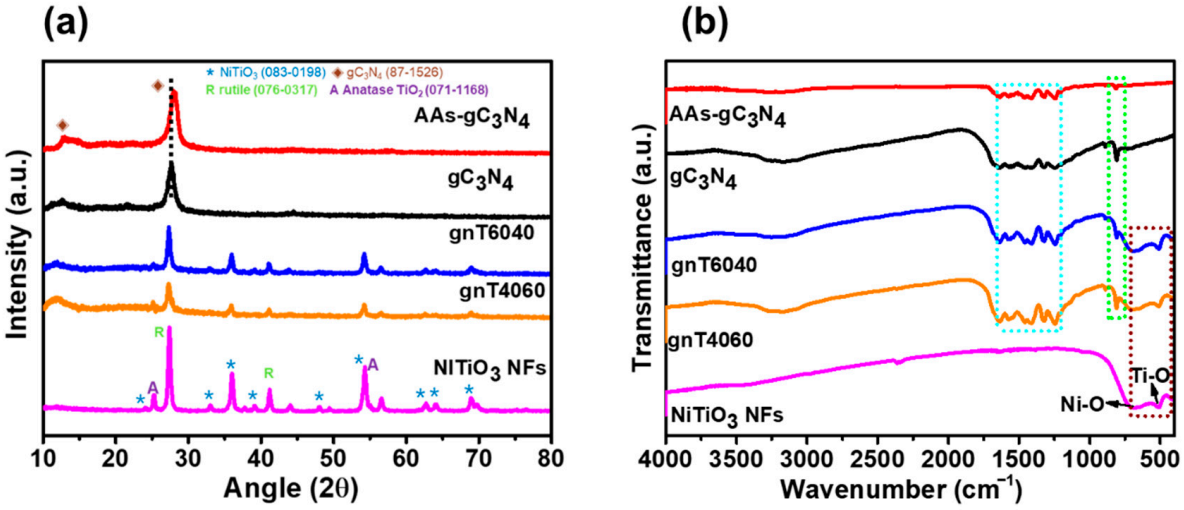

Figure 3. (**a**) X-ray diffraction (XRD) patterns and (**b**) Fourier transform infrared (FTIR) spectra of $NiTiO_3$ NFs, gC_3N_4, AAs-gC_3N_4, gnT4060, and the gnT6040 hybrid.

2.5. Surface Area and Pore Size Distribution

The effect of loading exfoliated and porous sheets of AAs-gC_3N_4 on the surface of 1D $NiTiO_3$ NFs was assessed by measuring the N_2 adsorption-desorption isotherms and the Barrett-Joyner-Halenda (BJH) pore size distribution of the pure and hybrid samples (Figure 4). The samples were degassed overnight (12 h) at 100 °C in vacuum condition. All samples displayed H3 hysteresis and the type-IV isotherm (Figure 4a), which indicated the presence of mesopores. The calculated Brunauer-Emmett-Teller (BET) surface areas of $NiTiO_3$ NFs, gC_3N_4, AAs-gC_3N_4 and gNT6040 at 0.5–1.0 P/P_0 were 11.048, 11.681, 126.84 and 46.0890 $m^2\ g^{-1}$, respectively. The enhanced surface area of the gnT6040 sample was approximately four-fold higher than that of the $NiTiO_3$ NFs and bulk gC_3N_4. This was attributed to the introduction of porous sheets of AAs-gC_3N_4 on the $NiTiO_3$ NFs; sheets of AAs-gC_3N_4 had a higher specific surface area compared with bulk gC_3N_4 (Table S1). Using the BJH method (Figure 4b), the pore volume of the hybrid structure (0.2279 $cm^3\ g^{-1}$) was six-times higher than that of pristine $NiTiO_3$ NFs (0.0357 $cm^3\ g^{-1}$). This analysis suggested that the porous hybrid structure, with its greater number of accessible active sites, was responsible for the improved photocatalytic performance. It should also be pointed out that in comparison with AAs-gC_3N_4 (126.84 $m^2\ g^{-1}$), the hybrid structure gnT6040 (46.08 $m^2\ g^{-1}$) showed a lower specific surface area, but higher photoactivity. Lower surface area could be due to a higher amount of $NiTiO_3$ NFs (60 wt%) in the hybrid structure as compared to AAs-gC_3N_4 (40 wt%). Also, this observation is an indirect indication that the dynamics process of photoinduced charge transfer occurring through the interface between AAs-gC_3N_4 and $NiTiO_3$ NFs may be crucial to the photocatalytic activity. Successful charge transfer occurring in the heterostructure interface is also confirmed by PEC and PL analysis.

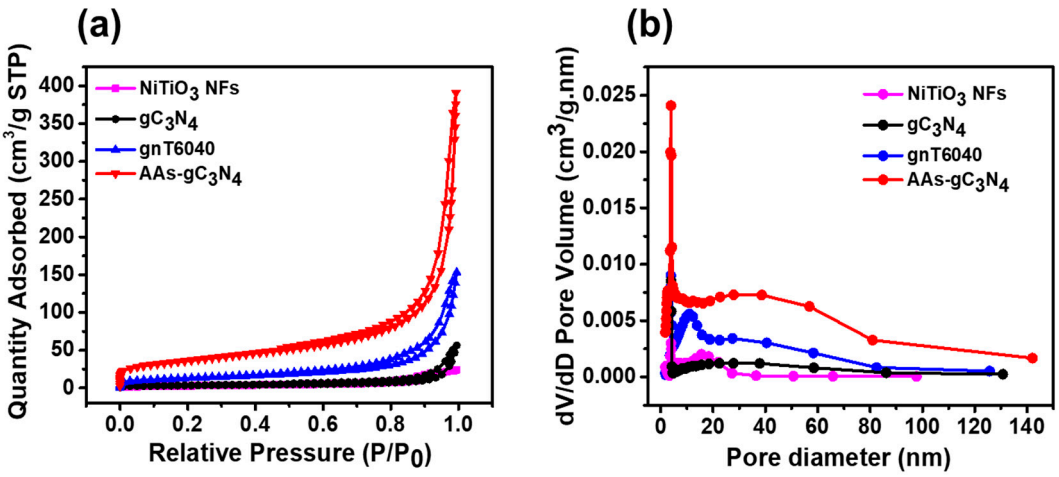

Figure 4. Brunauer-Emmett-Teller (BET) specific surface areas. (**a**) N_2 adsorption-desorption isotherms and (**b**) pore size distribution of $NiTiO_3$ NFs, gC_3N_4, AAs-gC_3N_4, and gnT6040.

2.6. X-ray Photoelectron Spectroscopy (XPS) Analysis

XPS was used to investigate the chemical states and elemental composition of the samples. The survey spectra (Figure S3) show that the main elements on the surface of $NiTiO_3$ NFs are Ni, Ti, O, and some amount of external carbon contaminant and the main elements of AAs-gC_3N_4 are C, N, and adsorbed O. The as-prepared gnT6040 was composed of $NiTiO_3$ NFs and AAs-gC_3N_4. XPS spectra of gnT6040 were further analyzed (Figure 5) to investigate the chemical states of its elements and the interaction between $NiTiO_3$ NFs and AAs-gC_3N_4. The Ni 2p signal (Figure 5a) appeared as a doublet at 855.45 and 873.38 eV, which were attributed to 2p3/2 and 2p1/2 states, respectively. Two broad peaks at 861.38 and 880.98 eV were assigned as Ni^{2+} satellites. In the Ti 2p spectra (Figure 5b), peaks at 458.28 (2p3/2) and 464.37 eV (2p1/2) were assigned to the Ti^{4+} oxidation state and those at 457.44 and 463.80 eV to the Ti^{3+} state. The appearance of the Ti–N peak at 458.93 eV indicated a strong interaction between Ti from $NiTiO_3$ NFs and N from the AAs-gC_3N_4 skeleton [28,29]. The formation of this Ti–N linkage decreased the recombination rate of photogenerated charges in the hybrid structure due to higher charge separation efficiency.

The O 1s peak (Figure 5c) was deconvoluted into three peaks, with the major one at 529.47 eV assigned to O^{2-} in the $NiTiO_3$ NFs structure. The peak at 532.68 eV resulted from the ×OH radicals adsorbed on the surface of $NiTiO_3$ NFs, while the peak appearing at 530.57 eV was attributed to lattice O^{2-} groups. The C 1s peak was deconvoluted into four peaks (Figure 5d) having binding energies at 284.29, 285.40, 287.91, and 288.79 eV, which were assigned to C–C, C–NH_2, C–$(NH)_x$, and N–C=N bonds, respectively. The N 1s signal was also deconvoluted into three peaks. The peaks at 398.48 and 399.72 eV were derived from sp^2-hybridized N atoms (C=N–C) and tertiary N atoms (N–C_3), respectively. The peak at 400.68 eV was assigned to the amino group (C–N–H) (Figure 5e). Another small peak at 396.75 eV corresponded to the Ti–N peak linkage between $NiTiO_3$ NFs and AAs-gC_3N_4 [27,28]. Thus, the overall XPS analysis indicated the successful formation of the $NiTiO_3$/AAs-gC_3N_4 composite with strong interaction between $NiTiO_3$ NFs and AAs-gC_3N_4. The XPS results were consistent with the SEM, TEM, X-ray diffraction, and FT-IR analyses confirming the formation of the heterostructure between $NiTiO_3$ NFs and AAs-gC_3N_4 nanosheets.

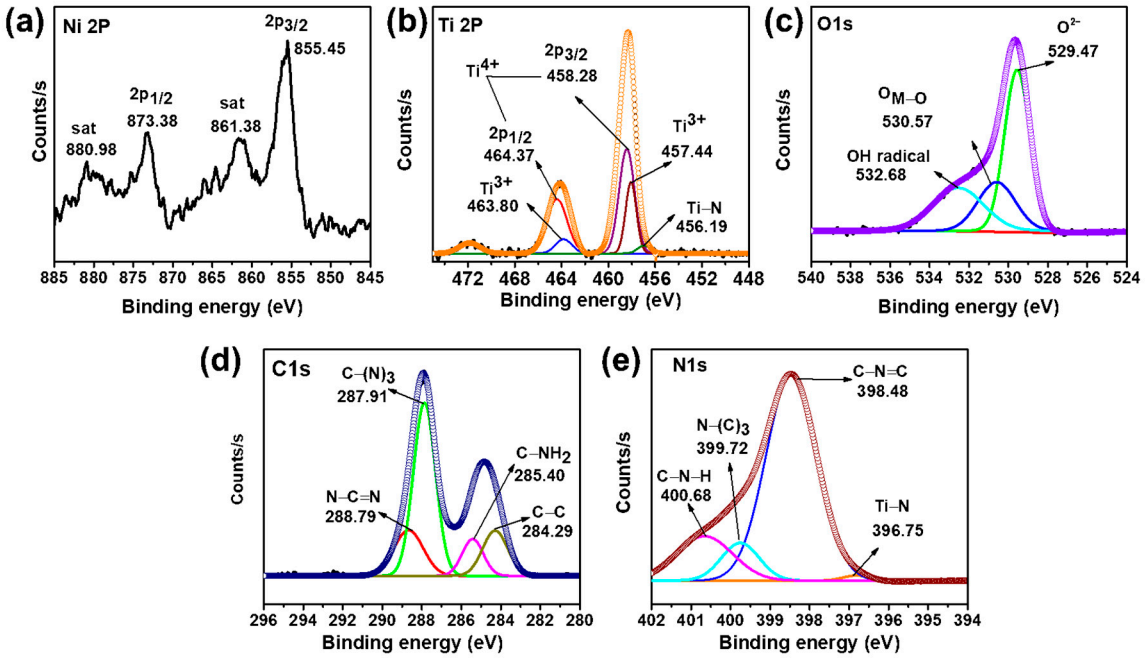

Figure 5. X-ray photoelectron spectra (XPS) of the gnT6040 hybrid sample with high-resolution spectra for (**a**) Ni 2p, (**b**) Ti 2p, (**c**) O 1s, (**d**) C 1s, and (**e**) N 1s signals.

2.7. Optical Absorbance

The light-harvesting capacity and bandgap energy of the pristine and hybrid photocatalysts were measured by analyzing their ultraviolet-visible (UV-vis) absorbance spectra (Figure 6a,b). The absorption band edges of pure $NiTiO_3$ NFs and gC_3N_4 were observed at approximately 430 and 400 nm, respectively. The composite structures extended the absorbance to the visible region from 450 to 900 nm due to the introduction of porous and thin sheets of AAs-gC_3N_4 between the $NiTiO_3$ NFs. The observed progressive color change of the different photocatalysts resulted from multiple reflections of incident light and was attributed to the porous framework (Figure 6a inset). The slight blue shift noted in the intrinsic absorption edge of the hybrid structure compared with bulk gC_3N_4 suggested the quantum confinement effect [30]. Bandgap energies calculated from the Kubelka-Munk function increased slightly from 2.38 eV for bulk gC_3N_4 to 2.41 eV for the hybrid structure. These changes in the band edge absorption indicated the ability of the photocatalysts to absorb light in the visible range. It is well-known that enhanced surface area, a porous framework, and increased bandgap are beneficial to light absorption, charge separation, and mass transfer and lead to improved photocatalytic properties. Furthermore, the increasing bandgaps from bulk gC_3N_4 to AAs-gC_3N_4 were also confirmed by a hypsochromic shift of the photoluminescence spectra (Figure 6c).

2.8. Photoluminescence (PL) Analysis

Charge carrier recombination is one of the most serious issues in photocatalysis. We analyzed the room-temperature photoluminescence (PL) emission spectra to determine the effective charge separation and transport in the pristine and hybrid structures (Figure 6c). PL was measured at an excitation wavelength of 325 nm. The strongest emission peak at 490 nm for gC_3N_4 indicated a high rate of carrier recombination which was further reduced in AAs-gC_3N_4. When AAs-gC_3N_4 was added to $NiTiO_3$ NFs, remarkable peak quenching was observed. This remarkable reduction in the intensity of the PL peak for the hybrid structure relative to that of bulk gC_3N_4 indicated a much lower photogenerated charge carrier recombination rate. Pure $NiTiO_3$ NFs showed much weaker PL emission (Figure S4) due to the lesser number of photogenerated charge carriers. Thus, PL analysis revealed

that the hybrid structures exhibited fewer recombination losses compared with the pristine photocatalysts. Quantum confinement was also corroborated by the PL peak shifting from 490 to 460 nm.

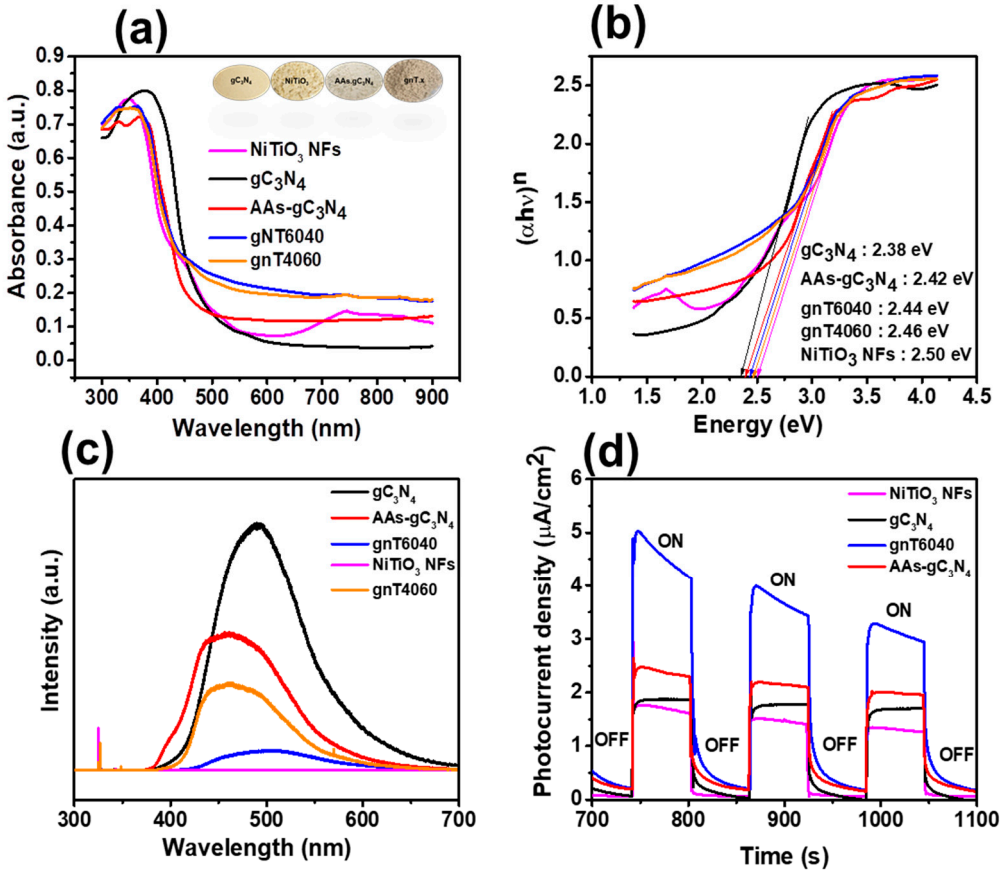

Figure 6. (**a**) Absorbance, (**b**) bandgap energy, (**c**) photoluminescence, and (**d**) transient photocurrent density of $NiTiO_3$ NFs, gC_3N_4, AAs-gC_3N_4, and gnT6040 hybrid photocatalyst.

2.9. Photoelectrochemical Performance

An efficient photocatalyst absorbs incident photons efficiently, converts them into photogenerated charge carriers (electrons and holes), and keeps them separated to successfully participate in surface reactions. This ability of the photocatalyst can be evaluated by measuring the transient photoresponse. In our study, we analyzed the intensity of photocurrent generated from pristine $NiTiO_3$ NFs, gC_3N_4, AAs-gC_3N_4, and the optimum hybrid structure (gnT6040) during several one-minute on/off cycles of light irradiation (Figure 6d). The intensity of photocurrent showed by the hybrid structure was much higher than the separate $NiTiO_3$ NFs, gC_3N_4, and AAs-gC_3N_4 photocatalysts. This enhanced photocurrent in the hybrid structure indicated that the presence of abundantly available charge carriers for rapid photocatalytic activity. This behavior also discovered a strong interaction between $NiTiO_3$ NFs and AAs-gC_3N_4 sheets and low interfacial transfer and separation of photogenerated charges via heterojunction formation. These results also reinforced the minimal recombination losses revealed by the PL analysis.

2.10. Removal of MB Dye

The water treatment capabilities of the pristine and the hybrid photocatalysts were evaluated using percentage removal of MB as a model pollutant under visible light irradiation (Figure 7). In this experiment, the removal of MB dye molecules was analyzed via an adsorption process. In the experiment, MB removal was measured by maintaining the

MB suspension in the dark for one hour with constant stirring. This hour-long stirring period ensured adsorption equilibrium before light irradiation. A controlled MB removal experiment was carried out without adding any catalysts to assess the stability (photolysis) of MB. As observed, change in the MB concentration was negligible initially when there was no catalyst added in the solution. This confirms that MB was stable under visible light for up to 1 h. However, adding catalyst significantly decreased the MB concentration. The MB removal performance of pristine $NiTiO_3$ NFs (72%), gC_3N_4, (76%), and AAs-gC_3N_4 (82%) was much poorer (Figure 7a) due to their poor optical properties and higher charge carrier recombination rates. When the $NiTiO_3$ NFs were combined with AAs-gC_3N_4 sheets, the MB removal rate increased substantially. The MB removal percentage of 97% was higher for the optimal photocatalyst gnT6040. These results showed that the gnT6040 hybrid was the best photocatalyst for water treatment. Moreover, the obtained MB removal performance was substantially better than that of reported $NiTiO_3/gC_3N_4$-based hybrid photocatalysts (Table S2). This improvement in photocatalytic performance observed with the hybrid structure was attributed to heterojunctions between the $NiTiO_3$ NFs and the porous AAs-gC_3N_4 sheets. These heterojunctions hampered charge carrier recombinations while providing abundant catalytically active sites.

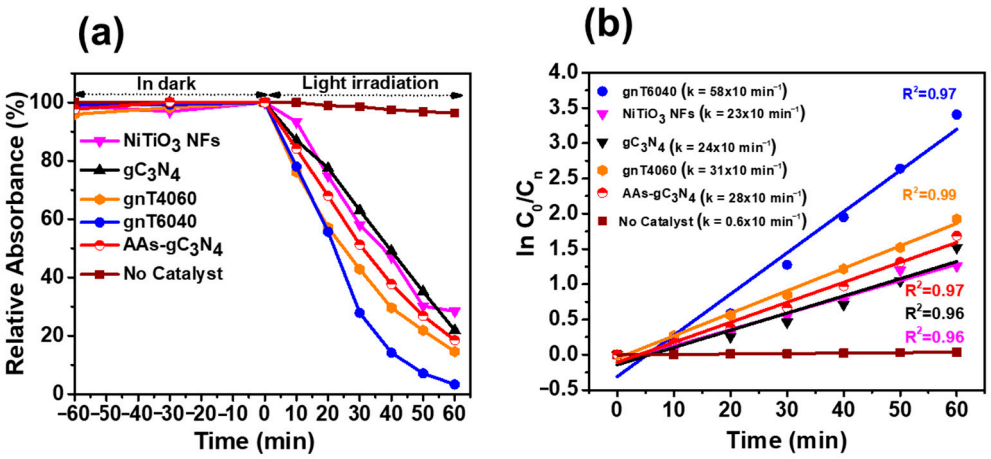

Figure 7. MB removal performance of $NiTiO_3$ NFs, gC_3N_4, AAs-gC_3N_4, and hybrid structures. (**a**) MB removal efficiency as a function of time and (**b**) reaction rate constants for the specified photocatalysts.

The reaction kinetics involved during the removal of MB was determined by measuring the first-order reaction equation of ln (C_0/C_n) as a function of kt, where k shows the slope of this curve corresponding to the apparent kinetic rate constant (Figure 7b). The apparent rate constant of gnT6040 was 58×10^{-3} min^{-1}, which is 1.8 times higher than that of pristine AAs-gC_3N_4 (28×10^{-3} min^{-1}), 2.5-fold higher than that of pristine $NiTiO_3$ NFs (23×10^{-3} min^{-1}), and 2.4-fold higher than that of bulk gC_3N_4 (24×10^{-3} min^{-1}). The higher performance of the hybrid structure may have resulted from higher charge carrier separation at the interfacial region and a broader range of light absorbance in the visible region. At lower AAs-gC_3N_4 content (gnT6040), a good dispersion of AAs-gC_3N_4 nanosheets on $NiTiO_3$ NFs could be formed. However, excess AAs-gC_3N_4 loading (gnT4060) causes a reduction of light for the covered $NiTiO_3$ NFs and decreases its excitation process for interfacial charge transfer. Therefore, a balance would be built between AAs-gC_3N_4 loading amount and $NiTiO_3$ NFs contact area, which can maximize the photocatalytic performance for the heterostructure. Through the sequential remediation of heterojunction components ($NiTiO_3$ NFs and AAs-gC_3N_4), we concluded an optimal loading of 40 wt% AAs-gC_3N_4 onto $NiTiO_3$ NFs, which exhibited the highest photocatalytic activity in our work.

In comparison, we also prepared and analyzed the MB removal efficiency of the p-gnT6040 sample prepared through physically mixing $NiTiO_3$ NFs and AAs-gC_3N_4 (Figure S6). Results showed that only 75% MB was removed by p-gnT6040 prepared

through physical mixing in comparison with the 97% MB removal efficiency of gnT6040. This analysis shows an interface was formed for gnT6040 while a physically mixed sample (p-gnT6040) does not.

2.11. Photocatalytic hydrogen evolution

To further explore their photocatalytic efficiency, the as-prepared samples were also evaluated in the water-splitting application under light irradiation. Figure 8 shows the detailed H_2 evolution performance of the photocatalysts over several cycles. The H_2 evolution experiment was performed in an aqueous triethanolamine (TEOA) solution (10 vol%) as the sacrificial agent. Hydrogen evolution was lower for bulk gC_3N_4 (50 μmol g^{-1}), AAs-gC_3N_4 (60 μmol g^{-1}), and $NiTiO_3$ NFs (47 μmol g^{-1}) because of their moderate photocatalytic properties compared with the hybrid photocatalyst gnT6040 (152 μmol g^{-1}) (Figure 8a). When we calculated the efficiency of the photocatalysts, the highest H_2 yield for gnT6040 (21.7 μmol g^{-1} h^{-1}) was 2.5-, 3.2- and 3-fold higher than that of AAs-gC_3N_4 (8.5 μmol g^{-1} h^{-1}), $NiTiO_3$ NFs (6.7 μmol g^{-1} h^{-1}), and gC_3N_4 (7.1 μmol g^{-1} h^{-1}), respectively (Figure 8b). This trend is the same as that observed for the MB removal test. The higher H_2 evolution performances recorded for the hybrid structures were ascribed to heterojunctions between the $NiTiO_3$ NFs and the porous AAs-gC_3N_4 sheets. These heterojunctions successfully hampered charge carrier recombination and hence helped enhance photocatalytic activity.

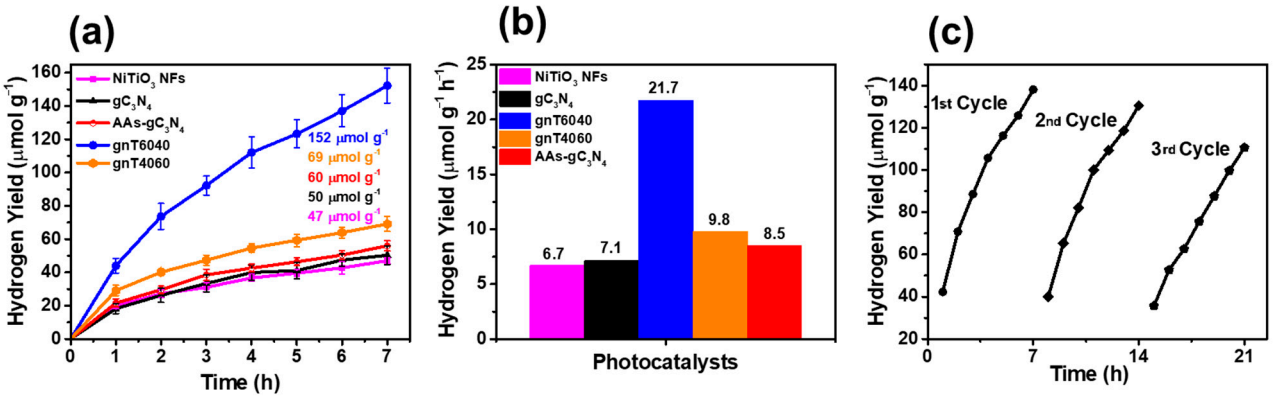

Figure 8. Photocatalytic H_2 evolution results measured in (**a**) μmol g^{-1} and (**b**) μmol g^{-1} h^{-1}. (**c**) Reusability evaluation of gnT6040.

For any efficient photocatalyst to be used in commercial applications, its stability and reusability are crucial. To evaluate the stability of the optimal gnT6040 photocatalyst, H_2 evolution experiments were carried out three times keeping the same conditions (Figure 8c). After each cycle, the vessel was purged with N_2 gas for 4 h and Ar. for 30 min to ensure an anaerobic environment. The experiment was then run again, and the evolved H_2 was collected and measured. The absence of a significant change in the performance of the photocatalyst in terms of H_2 evolution indicated good stability, which could be due to the incorporation of photo corrosion-reducing Ni [15]. Based on these results, gnT6040 showed efficient and stable photocatalytic performance and could be used for long-term applications.

3. Possible Photocatalytic Mechanism

A possible mechanism for the photocatalytic activity including MB removal and H_2 evolution for the $NiTiO_3$/AAs-gC_3N_4 photocatalyst is proposed based on our findings (Figure 9). In any photocatalytic activity, charge generation and effective utilization are very important and play a vital role in photocatalytic reactions. We observed that heterostructure formation between $NiTiO_3$ NFs and AAs-gC_3N_4 amorphous sheets increased the number of catalytically active sites, thereby increasing optical absorbance and charge separation

and substantially improving photocatalytic performance. The outstanding charge transfer in the hybrid structure was ascribed to the 1D $NiTiO_3$ NFs anchored on 2D amorphous nanosheets of AAs-gC_3N_4. When the light was illuminated on the heterostructure, electron-hole pairs were generated in the AAs-gC_3N_4 sheets. The energy levels of the $NiTiO_3$ NFs and AAs-gC_3N_4 were appropriate for charge transfer and separation at the interface. In our heterostructural photocatalytic system, AAs-gC_3N_4 acted as a light sensitizer owing to its narrow bandgap. As a result of light absorption, electrons from the valence band (VB) of amorphous AAs-gC_3N_4 excited into the conduction band (CB), leaving holes in VB. Due to suitable energy levels, these photoexcited electrons transferred from the CB of AAs-gC_3N_4 sheets to the CB of $NiTiO_3$ NFs via interfacial interactions. There, these CB electrons participate in surface reactions reacting with O_2 adsorbed on the catalytic surface to generate reactive oxygen species (ROS) i.e., $\times O_2^-$ and $\times$OH. These ROS are then responsible for productive surface reactions including removal of MB dye or enabling reduction for H_2 evolution reactions (Figure 9; I, II). Meantime, holes available in the VB of AAs-gC_3N_4 reacted with water (H_2O) molecules to make $\times$OH radicals that could oxidize pollutants. This favorable charge transfer mechanism at the interface of $NiTiO_3$ NFs and AAs-gC_3N_4 facilitated the efficient separation of photogenerated charge carriers (electrons and holes).

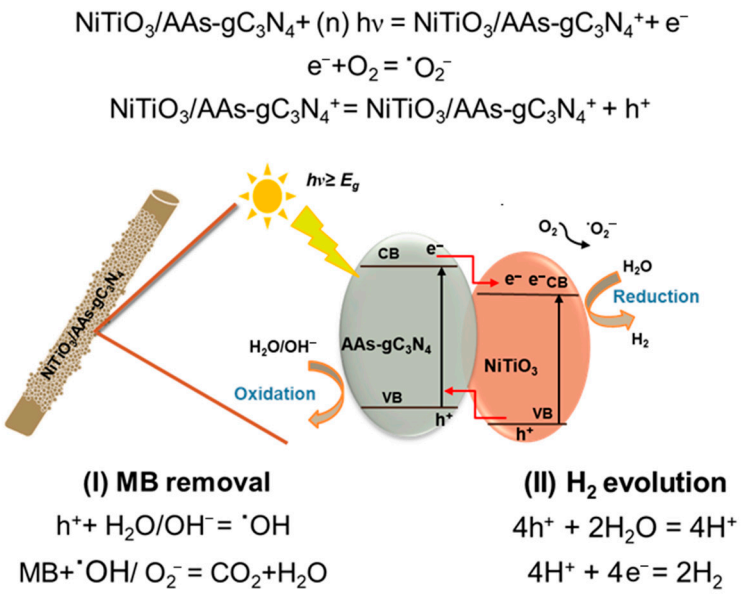

Figure 9. Proposed mechanism of photogeneration and transport of charge carriers at the interface of the $NiTiO_3$ NFs and AAs-gC_3N_4 heterostructures.

4. Materials and Methods

4.1. Materials

All the reagents utilized in our work were of analytical grade and were used as received. Titanium (IV) butoxide, acetylacetone (Reagent plus® grade, ≥99% purity), and nickel acetate tetrahydrate (98%) were purchased from Sigma-Aldrich (St. Louis, MO, USA). Polyvinylpyrrolidone (PVP)-K90 from Wako Pure Chemical Industries (Osaka, Japan) was used in the synthesis of the $NiTiO_3$ NFs. Melamine $C_6H_6N_6$ (1,3,5- triazine-2,4,6- triamine) was used to prepare gC_3N_4 powder. Methylene blue (Daejung Chemical & Metals, Siheung, Korea) was selected as the model pollutant. Acetic acid (AA) used in the exfoliation of melamine was also purchased from Daejung Chemical & Metals, Siheung, Korea. Sodium sulfate (Na_2SO_4) and TEOA were purchased from Samchun Chemicals (Pyeongtaek-si, Korea) to evaluate the photoresponse properties of transient photocurrent and H_2 evolution, respectively. Conductive fluorine-doped tin oxide (FTO) glass (15 mΩ) was used as the substrate to fabricate the films.

4.2. Synthesis of $NiTiO_3$ NFs

$NiTiO_3$ NFs were prepared through electrospinning. The solution for electrospinning was prepared by mixing 2 g titanium butoxide (TBOT) with 5 mL ethanol under constant stirring at room temperature. Then, nickel acetate tetrahydrate (1.5 wt%) was added and taken, and dissolved completely with continuous stirring. Polyvinylpyrrolidone (0.7 g) powder was taken and dissolved (8 h) in the above solution to get a viscous gel, and finally, 0.6 mL acetylacetone was added to increase the viscosity of the solution. A uniform light-green colored gel was formed after 2 h of vigorous stirring. This solution gel was transferred into a 12-mL nonpyrogenic plastic syringe connected to a 25-gauge (diameter: 0.26 mm) stainless-steel needle. Then, the syringe was mounted vertically with a pump that was connected to a high-voltage power supply. The flow rate of the solution through the syringe was maintained at 10 μL min^{-1} (Figure S2). Spinning was performed using an electrospinning system (NanoNC, Geumcheon-gu, Seoul, Korea) operating at 20 kV. The distance from the flat collector to the needle was fixed at 110 mm. The $NiTiO_3$ NF mats were collected every 3 h and dried in a vacuum oven (60 °C for 12 h) to evaporate the residual solvent. The dried fiber mats were finally sintered at 600 °C for 4 h in the air (ramp rate 10 °C/min).

4.3. Preparation of gC_3N_4

gC_3N_4 was synthesized by thermal polycondensation of melamine. Melamine powder (20 g) was placed in a covered alumina crucible and heated at 550 °C for 4 h at 3 °C min^{-1} in a muffle furnace. The yellow product was collected and crushed into a powder.

4.4. Preparation of AAs-gC_3N_4

Porous nanosheets of gC_3N_4 were synthesized by exfoliating bulk gC_3N_4 via acetic acid (AA) treatment followed by sintering. Sintering of gC_3N_4 pretreated in an acid environment tends to provide porous gC_3N_4 via pyrolysis of protonated melamine [31]. Under the optimized experimental conditions, 2 g bulk gC_3N_4 was added to 50 mL deionized water and ultrasonicated for 40 min. Then, 1 mL AA was added, and the solution was stirred for 3 h. This solution was washed several times with deionized water and ethanol until it reached pH 7. The washed, AA-treated gC_3N_4 nanosheets were dried overnight at 60 °C in a vacuum oven. Then, 0.2 g dried powder was sintered at 550 °C with 3 °C min^{-1} for 2 h (Figure S2). We denoted these AA-treated exfoliated and etched nanosheets as AAs-gC_3N_4. They were used without further treatment.

4.5. Preparation of $NiTiO_3$/AAs-gC_3N_4 Hybrids

Hybrid structures were synthesized according to our previous study [26]. In this experiment, a simple two-step process, as shown in Scheme 1 was used to fabricate hybrid photocatalysts. Firstly, a specific amount of $NiTiO_3$ NFs was dispersed in 50 mL ethanol under stirring at room temperature and then the required amount of AAs-gC_3N_4 powder was added to the $NiTiO_3$ NFs solution with constant stirring for 1 h. After proper mixing, the mixture solution was ultrasonicated (30-s pulse, 55% amplitude) for 40 min. The hybrid powder was collected by centrifuging the solution at 5000 rpm for 5 min and then dried the obtained powder in a vacuum oven. In the second step, these dry hybrid powders were sintered at 300 °C for 2 h (10 °C/min) in an N_2 atmosphere to ensure strong interaction between $NiTiO_3$ NFs and AAs-gC_3N_4 [32]. The final samples (dark grey) were carefully collected soon after the box furnace had reached room temperature. The as-synthesized heterostructures were identified as $NiTiO_3$/AAs-gC_3N_4 60/40 (gnT6040) and $NiTiO_3$/AAs-gC_3N_4 40/60 (gnT4060).

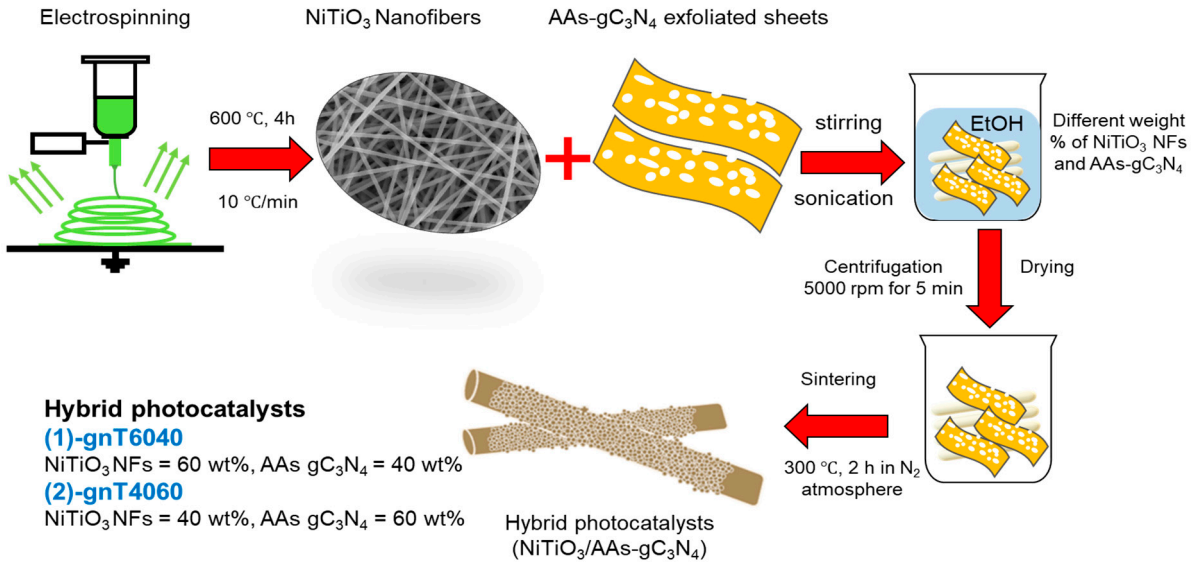

Scheme 1. Schematic illustration of the fabrication of gnTx heterostructures.

4.6. Photoelectrochemical Performance

The transient photocurrent density was measured in the dark and under UV-vis light irradiation using a three-electrode quartz cell and a potentiostat (VersaSTAT 4; Princeton Applied Research, Oak Ridge, TN, USA) in 0.5 M sodium sulfate electrolyte. The working electrode was prepared by dispersing a 0.2 g powder sample in 1.5 mL ethanol and then spin-coating onto the FTO substrate. The coated FTO substrates were dried in an oven at 60 °C for 2 h and sintering at 150 °C for 1 h. A prepared photoresponsive film, Ag/AgCl, and Pt wire were used as the working, reference, and counter electrodes, respectively. Various one-minute long off/on cycles were noted over several minutes of irradiation with UV-vis light from a 300 W Xe-arc lamp (66984; Newport Corporation, Yongin-Si, Korea).

4.7. MB Removal Test

To measure the photocatalytic performance of the pristine and hybrid catalysts, the MB removal test was evaluated. Visible light was irradiated on an aqueous solution of MB model pollutant placed in a batch-type indigenous-made reactor. In this MB removal experiment, the required amount of the photocatalyst (0.1 g) was dispersed in a 250 mL MB solution of 3.2 mg L^{-1} concentration. This solution was kept in dark with constant stirring and three sample aliquots were taken and recorded as −60, −30, and 0 min. This stirring in dark and at room temperature helps the solution achieve adsorption-desorption equilibrium. After equilibrium was attained, the suspension was irradiated with visible light (100 W halogen lamp, 380–800 nm) under constant stirring (120 rpm). During light irradiation, 6-mL sample aliquots of the solution were collected after every 10-min interval for analysis; their absorbance corresponded to the concentration of MB in the solution. The extent of pollutant removal was determined by the change in optical absorbance at 663 nm.

4.8. Hydrogen Evolution

The hydrogen evolution performance of the pristine and hybrid photocatalysts was evaluated by using a quartz reactor. In a particular experiment, 10 mg photocatalyst was added to a 10 vol% aqueous solution of TEOA. After complete dispersion of the sample powder, the suspension was shifted into a quartz reactor (in-house made), which was then made air-tight using rubber septum. Nitrogen and argon gases were purged into the reactor to create a completely anaerobic environment. Subsequently, a Xe lamp placed 6cm away from the reactor was used to irradiate the suspension. The suspension was irradiated up to 7 h and then the produced gas (260 µL) was collected after every 1 h intervals using a

syringe (500 µL, Agilent, Santa Clara, CA, USA). Thus, gas produced is quantified by using gas chromatography (model 6500GC; YL Instruments, Anyang, Korea). This procedure is repeated for every sample.

4.9. Characterization

The surface morphologies of the samples were analyzed using an FE-SEM operating at 15 kV (S4800; Hitachi, Tokyo, Japan). Additional details were provided by a scanning TEM operating at 200 kV (JEM-2100F; JEOL, Tokyo, Japan). Phase analysis of the pure and hybrid samples was made by X-ray diffraction (D/Max-2500/PC (Cu Kα source, λ = 1.5418 Å); Rigaku, Tokyo, Japan). Chemical binding energies were determined by XPS (K-Alpha$^+$ (Al Kα source); Thermo Fisher Scientific, Waltham, MA, USA). The chemical interactions at the surface of the photocatalyst were characterized by FT-IR (iS10; Thermo Fisher Scientific) over the range of 400–4000 cm^{-1}. Ultraviolet-visible spectroscopy (V650; Jasco, Hachioji-shi, Tokyo, Japan) was used to measure the optical absorbance, which is related to the bandgap energy. The separation of charge carriers and their recombination were analyzed by measuring the PL emission spectrum using a spectrofluorometer (SC-100; Dongwoo, Pyeongtaek-si, Gyeonggi-do, Korea) using an excitation wavelength of 325 nm. The BET method was used to measure the specific area of the photocatalysts according to their N_2 adsorption-desorption isotherms using a Quantachrome system (Autosorb iQ-C; Quantachrome Instruments, Boynton Beach, FL, USA). The total pore size distribution was determined by the BJH method.

5. Conclusions

In this work, noble-metal-free, visible-light-active photocatalysts based on heterojunctions of $NiTiO_3$ NFs and holey AAs-gC_3N_4 with different compositions were synthesized. The $NiTiO_3$ NFs sensitized with the porous nanosheets exhibited enhanced photocatalytic performance. This enhancement by the 1D/2D heterostructure was ascribed to swift charge transport, higher light absorbance, and effective separation of the charge carriers from the barrier potential produced at the interface. Moreover, a dramatic reduction of recombination losses by the hybrid sample was confirmed by room-temperature PL and photocurrent response measurements. The superior performance of the AAs-gC_3N_4-sensitized $NiTiO_3$ NFs photocatalyst was also due in part to its large BET surface area and abundance of catalytically active sites. Overall, the results and facile synthesis method offer an exciting avenue for the design of cost-effective catalysts for use in photocatalytic applications.

Supplementary Materials: The following are available online at https://www.mdpi.com/2073-4344/11/3/385/s1, Figure S1: SEM (EDS) of gnT6040 and pure AAs-gC_3N_4, Figure S2: Detailed experimental setups of $NiTiO_3$ NFs, gC_3N_4, and AAs-gC_3N_4, Figure S3: XPS survey spectra of $NiTiO_3$ NFs, AAs-gC_3N_4 and gnT6040, Figure S4: PL spectra of pure $NiTiO_3$ NFs, Figure S5: TEM mapping of gnT6040 hybrid structure, Figure S6: MB removal efficiency of the p-gnT6040 sample prepared through physical mixing, Table S1: BET specific surface areas of all samples, Table S2: Literature of MB removal of photocatalysts containing $NiTiO_3$.

Author Contributions: H.K. performed the experiments and wrote a draft of the paper, S.K. provided very helpful technical assistance during experiments and critical data analysis. C.S.L. supervised the overall work and polished the paper. All authors have read and agreed to the published version of the manuscript.

Funding: This research is funded by the National Research Foundation of Korea (NRF-2020K2A9A2A06071441, FY2020) and by the Industrial Technology Innovation Program of the Korea Evaluation Institute of Industrial Technology (KEIT) granted financial resource from the Ministry of Trade, Industry & Energy, Republic of Korea (No. 20012211).

Data Availability Statement: Data is contained within the article or Supplementary Material.

Conflicts of Interest: The authors declare no conflict of interest.

References

1. Katal, R.; Masudy-Panah, S.; Tanhaei, M.; Farahani, M.H.D.A.; Jiangyong, H. A review on the synthesis of the various types of anatase TiO_2 facets and their applications for photocatalysis. *Chem. Eng. J.* **2020**, *384*, 123384. [CrossRef]
2. Vallejo, W.; Cantillo, A.; Díaz-Uribe, C. Methylene Blue Photodegradation under Visible Irradiation on Ag-Doped ZnO Thin Films. *Int. J. Photoenergy* **2020**, *2020*, 1–11. [CrossRef]
3. Marcelino, R.B.P.; Amorim, C.C. Towards visible-light photocatalysis for environmental applications: Band-gap engineering versus photons absorption—a review. *Environ. Sci. Pollut. Res.* **2018**, *26*, 4155–4170. [CrossRef] [PubMed]
4. Perween, S.; Ranjan, A. Improved visible-light photocatalytic activity in $ZnTiO_3$ nanopowder prepared by sol-electrospinning. *Sol. Energy Mater. Sol. Cells* **2017**, *163*, 148–156. [CrossRef]
5. Subramanian, S.; Ganapathy, S.; Subramanian, S.; Rajaram, M.; Thangaraj, R.; Ramasamy, J. Effect of photocatalytic activity on cobalt titanate ($CoTiO_3$) nanostructures. *Mater. Today: Proc.* **2020**, *33*, 2274–2278. [CrossRef]
6. Konstas, P.-S.; Konstantinou, I.; Petrakis, D.; Albanis, T. Development of $SrTiO_3$ Photocatalysts with Visible Light Response Using Amino Acids as Dopant Sources for the Degradation of Organic Pollutants in Aqueous Systems. *Catal.* **2018**, *8*, 528. [CrossRef]
7. Lakhera, S.K.; Hafeez, H.Y.; Veluswamy, P.; Ganesh, V.; Khan, A.; Ikeda, H.; Neppolian, B. Enhanced photocatalytic degradation and hydrogen production activity of in situ grown TiO_2 coupled $NiTiO_3$ nanocomposites. *Appl. Surf. Sci.* **2018**, *449*, 790–798. [CrossRef]
8. Kumar, B.S.; Shanmugharaj, A.; Kalpathy, S.K.; Anandhan, S. Some new observations on the structural and phase evolution of nickel titanate nanofibers. *Ceram. Int.* **2017**, *43*, 6845–6857. [CrossRef]
9. Yuan, P.-H.; Fan, C.-M.; Ding, G.-Y.; Wang, Y.-F.; Zhang, X.-C. Preparation and photocatalytic properties of ilmenite $NiTiO_3$ powders for degradation of humic acid in water. *Int. J. Miner. Met. Mater.* **2012**, *19*, 372–376. [CrossRef]
10. Huang, Z.; Zeng, X.; Li, K.; Gao, S.; Wang, Q.; Lu, J. Z-Scheme $NiTiO_3$/g-C_3N_4 Heterojunctions with Enhanced Photoelectrochemical and Photocatalytic Performances under Visible LED Light Irradiation. *ACS Appl. Mater. Interfaces* **2017**, *9*, 41120–41125. [CrossRef]
11. Rono, N.; Kibet, J.K.; Martincigh, B.S.; Nyamori, V.O. A review of the current status of graphitic carbon nitride. *Crit. Rev. Solid State Mater. Sci.* **2020**, 1–29. [CrossRef]
12. Tahir, M.; Sagir, M.; Shahzad, K. Removal of acetylsalicylate and methyl-theobromine from aqueous environment using nano-photocatalyst WO_3-TiO_2 @g-C_3N_4 composite. *J. Hazard. Mater.* **2019**, *363*, 205–213. [CrossRef]
13. Opoku, F.; Govender, K.K.; Van Sittert, C.G.C.E.; Govender, P.P. Insights into the photocatalytic mechanism of mediator-free direct Z-scheme g-C_3N_4/Bi_2MoO_6(010) and g-C_3N_4/Bi_2WO_6(010) heterostructures: A hybrid density functional theory study. *Appl. Surf. Sci.* **2018**, *427*, 487–498. [CrossRef]
14. Wang, Z.; Peng, J.; Feng, X.; Ding, Z.; Li, Z. Wide spectrum responsive CdS/$NiTiO_3$/CoS with superior photocatalytic performance for hydrogen evolution. *Catal. Sci. Technol.* **2017**, *7*, 2524–2530. [CrossRef]
15. Wang, B.; Li, X.; Wu, H.; Xu, G.; Zhang, X.; Shu, X.; Lv, J.; Wu, Y. Synthesis of Ni−MoS x /g-C_3N_4 for Photocatalytic Hydrogen Evolution under Visible Light. *ChemCatChem* **2020**, *12*, 911–916. [CrossRef]
16. Li, Y.; Xu, J.; Peng, M.; Liu, Z.; Li, X.; Zhao, S. MoS_2/$NiTiO_3$ Heterojunctions as Photocatalysts: Improved Charge Separation for Promoting Photocatalytic Hydrogen Production Activity. *Catal. Surv. Asia* **2019**, *23*, 277–289. [CrossRef]
17. Qu, X.; Liu, M.; Zhang, W.; Sun, Z.; Meng, W.; Shi, L.; Du, F. A facile route to construct $NiTiO_3$/Bi_4NbO_8Cl heterostructures for enhanced photocatalytic water purification. *J. Mater. Sci.* **2020**, *55*, 1–13. [CrossRef]
18. Wang, Q.; Zhang, L.; Guo, Y.; Shen, M.; Wang, M.; Li, B.; Shi, J. Multifunctional 2D porous g-C_3N_4 nanosheets hybridized with 3D hierarchical TiO_2 microflowers for selective dye adsorption, antibiotic degradation and CO_2 reduction. *Chem. Eng. J.* **2020**, *396*, 125347. [CrossRef]
19. Israr, M.; Raza, F.; Nazar, N.; Ahmad, T.; Khan, M.F.; Park, T.J.; Basit, M.A. Rapid conjunction of 1D carbon nanotubes and 2D graphitic carbon nitride with ZnO for improved optoelectronic properties. *Appl. Nanosci.* **2020**, *10*, 1–13. [CrossRef]
20. Yang, B.; Bai, X.; Wang, J.; Fang, M.; Wu, X.; Liu, Y.; Huang, Z.; Lao, C.-Y.; Min, X. Photocatalytic Performance of NiO/$NiTiO_3$ Composite Nanofiber Films. *Catalysts* **2019**, *9*, 561. [CrossRef]
21. Wang, Y.; Du, P.; Pan, H.; Fu, L.; Zhang, Y.; Chen, J.; Du, Y.; Tang, N.; Liu, G. Increasing Solar Absorption of Atomically Thin 2D Carbon Nitride Sheets for Enhanced Visible-Light Photocatalysis. *Adv. Mater.* **2019**, *31*, e1807540. [CrossRef] [PubMed]
22. Shu, X.; He, J.; Chen, D. Visible-Light-Induced Photocatalyst Based on Nickel Titanate Nanoparticles. *Ind. Eng. Chem. Res.* **2008**, *47*, 4750–4753. [CrossRef]
23. Li, M.-W.; Yuan, J.-P.; Gao, X.-M.; Liang, E.-Q.; Wang, C.-Y. Structure and optical absorption properties of $NiTiO_3$ nanocrystallites. *Appl. Phys. A* **2016**, *122*, 1–7. [CrossRef]
24. Dharmaraj, N.; Park, H.; Kim, C.; Kim, H.Y.; Lee, D. Nickel titanate nanofibers by electrospinning. *Mater. Chem. Phys.* **2004**, *87*, 5–9. [CrossRef]
25. Kumar, S.; Karthikeyan, S.; Lee, A.F. g-C_3N_4-Based Nanomaterials for Visible Light-Driven Photocatalysis. *Catalysts* **2018**, *8*, 74. [CrossRef]
26. Pawar, R.C.; Kang, S.; Park, J.H.; Kim, J.-H.; Ahn, S.; Lee, C.S. Evaluation of a multi-dimensional hybrid photocatalyst for enrichment of H_2 evolution and elimination of dye/non-dye pollutants. *Catal. Sci. Technol.* **2017**, *7*, 2579–2590. [CrossRef]
27. Pham, T.-T.; Shin, E.W. Thermal formation effect of g-C_3N_4 structure on the visible light driven photocatalysis of g-C_3N_4/$NiTiO_3$ Z-scheme composite photocatalysts. *Appl. Surf. Sci.* **2018**, *447*, 757–766. [CrossRef]

28. Dao, D.Q.; Nguyen, T.K.A.; Pham, T.-T.; Shin, E.W. Synergistic Effect on Photocatalytic Activity of Co-Doped $NiTiO_3$/g-C_3N_4 Composites under Visible Light Irradiation. *Catalysts* **2020**, *10*, 1332. [CrossRef]
29. Pham, T.-T.; Shin, E.W. Inhibition of charge recombination of $NiTiO_3$ photocatalyst by the combination of Mo-doped impurity state and Z-scheme charge transfer. *Appl. Surf. Sci.* **2020**, *501*, 143992. [CrossRef]
30. Zhang, S.; Song, S.; Gu, P.; Ma, R.; Wei, D.; Zhao, G.; Wen, T.; Jehan, R.; Hu, B.; Wang, X. Visible-light-driven activation of persulfate over cyano and hydroxyl group co-modified mesoporous g-C_3N_4 for boosting bisphenol A degradation. *J. Mater. Chem. A* **2019**, *7*, 5552–5560. [CrossRef]
31. Chang, F.; Li, C.; Luo, J.; Xie, Y.; Deng, B.; Hu, X. Enhanced visible-light-driven photocatalytic performance of porous graphitic carbon nitride. *Appl. Surf. Sci.* **2015**, *358*, 270–277. [CrossRef]
32. Pham, T.-T.; Shin, E.W. Influence of g-C_3N_4 Precursors in g-C_3N_4/$NiTiO_3$ Composites on Photocatalytic Behavior and the Interconnection between g-C_3N_4 and $NiTiO_3$. *Langmuir* **2018**, *34*, 13144–13154. [CrossRef] [PubMed]